Geophysical Journal International

Geophys. J. Int. (2016) **204,** 1477–1489 doi: 10.1093/gji/ggv518

GJI Geomagnetism, rock magnetism and palaeomagnetism

Propagation and reflection of diffusionless torsional waves in a sphere

S. Maffei and A. Jackson

Institute of Geophysics, ETH–Sonneggstrasse 5, Zürich. E-mail: maffei.ste@gmail.com

Accepted 2015 November 26. Received 2015 November 25; in original form 2015 July 23

SUMMARY

We consider an inviscid and perfectly conducting fluid sphere in rapid rotation and permeated by a background magnetic field. Such a system admits normal modes in the form of torsional oscillations, namely azimuthal motions of cylinders coaxial with the rotation axis. We analyse this system for a particular background magnetic field that provides a new closed form normal mode solution. We derive Wentzel–Kramers–Brillouin–Jeffreys (WKBJ) approximations to the normal modes, and focus particularly on the reflections that take place on the rotation axis and at the equator. We propose a procedure to calculate the reflection coefficients and we discuss the analogy of our findings with well-known seismological results. Our analytical results are tested against numerical calculations and show good agreement.

Key words: Numerical approximations and analysis; Rapid time variations; Planetary interiors.

1 INTRODUCTION

An electrical conducting fluid flowing in a magnetic field, such as in the Earth's liquid outer core, can sustain magnetohydrodynamic waves. Such waves, also called Alfvén waves, as first mathematically formalised in Alfvén (1942), are described by oscillations of the fluid that are perpendicular to a background magnetic field. The bending of the magnetic lines due to the flow generates a magnetic tension that is the restoring force that leads to oscillatory motions. The resulting waves propagate along the lines of the background magnetic field with a velocity proportional to the field intensity.

Taylor (1963) and Braginsky (1970) were the first to show that in planetary interiors, axisymmetric motions could result in Alfvén waves supported by a background magnetic field perpendicular to the rotation axis of the planet. It is common to describe these waves in a cylindrical coordinate system (s, ϕ, z) with the vertical direction parallel to the rotation axis. In such a coordinate system the axisymmetric fluid flow $u_\phi(s)$ can bend the lines of the radial magnetic field B_s giving rise to a magnetic tension that tends to decelerate the original flow. The resulting oscillatory motion propagates along s and has an amplitude that is constant over the surface of cylinders whose axis is parallel to the rotation axis, called geostrophic cylinders. The geophysical importance of the torsional waves lies in the fact that their frequencies are proportional to the root mean square value of B_s^2 averaged over the geostrophic cylinders, implying that the detection of the fundamental period of these waves provides invaluable information about the intensity of the magnetic field inside the liquid core. In particular the period predicted by Braginsky (1970) for the torsional waves of about 60–80 yr, implied a root mean square value of B_s of 0.3 mT in the Earth's outer core.

There have been many attempts to detect torsional waves from observations. As first shown in Jault *et al.* (1988) and subsequently by Jackson *et al.* (1993) it is possible to calculate the length of day (LOD) variation due to the angular momentum carried by geostrophic motions in the core and successfully compare it with the geodetic observations. The comparison shows that the outer core flows inferred from geomagnetic observations can explain the 60–80 yr signal in the LOD variations, of the order of milliseconds, in agreement with the early prediction of Braginsky (1970). Hide *et al.* (2000) estimated the time-varying angular momentum carried by different geostrophic cylinders in the outer core. These authors found, for the period 1840–1990, evidence of angular momentum anomalies that they interpreted as torsional waves, propagating from the equator to the rotation axis with traveltimes of about 60 yr and approximately 65 yr periodicity. Once the waves reach the rotation axis, they seem to disappear, suggesting no reflection there. More recently, Gillet *et al.* (2010) employed a data assimilation approach using the geomagnetic field model *gufm1* of Jackson *et al.* (2000) as observations and performed an inversion tailored to the search for torsional waves with periods between 6 and 8 yr during the second half of the 20th century. Their results suggest the existence of coherent propagation of geostrophic velocities from the tangent cylinder (the imaginary geostrophic cylinder tangent to the inner core) in the directions of the rotation axis and the equator, without apparent reflection at these boundaries. The traveltime from the tangent cylinder to the equator is about 4 yr, with larger velocities in the bulk of the core than at the equator. The study of Gillet *et al.* (2010) shows the existence of torsional waves that have fundamental periods 10 times shorter than the previous estimates, and must therefore be supported by a magnetic field that is at least 10 times stronger in the interior than on the core–mantle boundary (CMB), in agreement with recent geodynamo simulations (e.g. Aubert *et al.* 2009). An ensemble inversion procedure similar to that of Gillet *et al.* (2010) has been employed in Gillet *et al.* (2015) to invert

the geomagnetic field model COV_OBS of Gillet *et al.* (2013) for quasi-geostrophic core surface flows. The authors introduced an inversion scheme that accounts for temporal covariances of model errors that allows for better resolution on decadal and interannual timescales. The geostrophic flow pattern extracted from the resulting flow model well reproduces the observed LOD on timescales from 4 to 9.5 yr for the period 1940–2010. The agreement is particularly good during the last decades, something that the authors attribute to the increasing number of good quality observations with time. The geostrophic flow pattern shows similar characteristics to the one derived in Gillet *et al.* (2010), namely the presence of pulses of geostrophic flow travelling from the tangent cylinder to the equator, a higher velocity of propagation at high to middle latitudes and an apparent lack of reflection at the equatorial boundary. However, the pattern seems to be in general less coherent than the one of Gillet *et al.* (2010) and the excitation of the pulses at the tangent cylinder also appear to be less regular. This can be attributed to the wider filter applied in Gillet *et al.* (2015) (4–9.5 yr instead of the 6–8 yr used in Gillet *et al.* (2010)) and to the more refined treatment of the temporal covariances in the model errors. It is worthwhile noting that the 6–8 yr geomagnetic signal, first discovered by Abarco del Rio *et al.* (2001), has also been suggested to be due to gravitational coupling between the inner core and the mantle, see Mound & Buffett (2003, 2005).

The aim of this study is to better understand the propagation of torsional waves, with particular focus on the reflections, both at the equator and at the rotation axis. In what follows we build on the work of Cox *et al.* (2014), in which initial pulses of geostrophic velocity are evolved in time according to the torsional wave evolution equation with prescribed background magnetic field; their propagation and reflection properties are then analysed. For a constant background field Cox and coauthors suggested that at any reflection from the rotation axis a change in phase is introduced, therefore altering the shape of the initial pulse. The phase shift resembles the $\pi/2$ phase shift introduced in seismic waves at any passage through a caustic, a phenomenon that is well known in seismology (Chapman 2004, section 7.2). In Cox *et al.* (2014) only the reflection at the rotation axis (that we address as a pseudo-reflection) in cylindrical domains is rigorously considered. We propose a methodology to derive the reflection coefficients for both boundaries in a spherical domain. In what follows we neglect any coupling mechanism with the mantle. A study of the core–mantle coupling mechanisms and their effects on torsional waves and LOD signal can be found in Mound & Buffett (2005, 2007).

This paper is structured as follows: In Section 2 we introduce the equation governing the torsional wave propagation in the ideal case. That is, we neglect viscous and ohmic dissipations and the coupling with the inner core and the mantle. In Section 3 we consider normal modes resulting from the constructive interference of torsional waves. We consider two different background magnetic fields: the constant one and a field that goes to zero at the equatorial boundary. The constant field has the advantage of supporting known normal modes: see Roberts & Aurnou (2012) and Cox *et al.* (2014). The spatially varying field that we introduce in this study has an interesting behaviour at the equator that helps us illustrate the meaning of the boundary conditions for the torsional waves. The waves propagating in these two background fields are illustrated in Section 4. The main results of the paper are derived in Section 5: here we introduce the WKBJ (Wentzel–Kramers–Brillouin–Jeffreys) expansion as a tool to obtain analytical approximations to the normal modes and to explain the propagation properties illustrated in Section 4. In particular, we derive reflection coefficients valid at both the rotation axis and the equator. Discussion of the results and conclusions are given in Section 6.

2 TORSIONAL WAVE EQUATION

We derive the wave equation for the diffusion-free torsional waves by considering the governing equations for an incompressible, inviscid, perfectly conducting fluid flowing with velocity $\mathbf{u}$ in the presence of a time-varying magnetic field $\mathbf{B}$:

$$\rho\frac{\partial \mathbf{u}}{\partial t} + \rho(\mathbf{u}\cdot\nabla)\mathbf{u} + 2\rho\boldsymbol{\Omega}\times\mathbf{u} = -\nabla P + \mathbf{J}\times\mathbf{B} \tag{1}$$

$$\frac{\partial \mathbf{B}}{\partial t} = \nabla\times(\mathbf{u}\times\mathbf{B}) \tag{2}$$

$$\nabla\cdot\mathbf{u} = 0 \tag{3}$$

$$\nabla\cdot\mathbf{B} = 0 \tag{4}$$

where ρ is the hydrostatic reference density, $\boldsymbol{\Omega}$ is the angular velocity vector of the Earth, P is the non-hydrostatic pressure and $\mathbf{J}$ is the current density, defined via Ampere's law $\mu_0\mathbf{J} = \nabla\times\mathbf{B}$. Eq. (1) is the inviscid version of the Navier–Stokes equation; (2) is the diffusion-free induction equation; (3) and (4) express the incompressibility condition of the velocity field and the solenoidal nature of the magnetic field, respectively. As mentioned above we work in a cylindrical coordinate system (s, ϕ, z) defined by the unit vectors $(\mathbf{e}_s, \mathbf{e}_\phi, \mathbf{e}_z)$, the vertical direction being defined by the rotation axis $\boldsymbol{\Omega} = \Omega\mathbf{e}_z$ and the origin is placed at the centre of our domain. Although the Earth's liquid core is usually represented as a spherical shell we work in a fully spherical domain of radius r_c. The reason is that of simplicity: the presence of the inner core is not important for the purpose of this paper. As shown in Mound & Buffett (2007), the presence of the inner core in the diffusionless case has only a minor effect on the geometry and frequency of the normal modes (see their figure A1). Care has to be taken, though, in interpreting the results derived here, since in the spherical shell, geostrophic waves hitting the tangent cylinder experience partial reflection resulting in less energy being transmitted inside the tangent cylinder as shown in Jault & Légaut (2005) and Cox *et al.* (2014). Furthermore, depending on the strength of the electromagnetic coupling between the fluid outer core and the solid inner core, the dynamics inside the tangent cylinder can be strongly coupled with the solid body rotation of the inner core, altering the shape of the torsional waves normal modes there (see Buffett & Mound 2005; Mound & Buffett 2007).

The physical boundary conditions that the vectors $\mathbf{u}$ and $\mathbf{B}$ need to satisfy are (1) non-penetration of the fluid across the CMB and (2) considering the mantle as an insulator, that the radial current density also vanishes there. Defining the normal to the surface of the spherical domain $\mathbf{n}$ these conditions are

$$\mathbf{n}\cdot\mathbf{u}|_{r=r_c} = 0 \tag{5}$$

for the velocity field and

$$\mu_0\mathbf{n}\cdot\mathbf{J}|_{r=r_c} = \mathbf{n}\cdot(\nabla\times\mathbf{B})|_{r=r_c} = 0 \tag{6}$$

for the magnetic field. We define a background state in which the fluid is at rest, $\mathbf{u}_0 = 0$, and there is a background magnetic field $\mathbf{B}_0 = (B_{s0}, B_{\phi 0}, B_{z0})$ satisfying insulating boundary conditions (6) and the

solenoidal condition (4). We define the velocity and magnetic field to be the sum of their background values and small perturbations $\mathbf{u}$ and $\mathbf{B}'$, respectively. Upon linearisation of (1) and (2) around the background state we obtain the system of equations governing the evolution of the perturbation fields. In line with Braginsky (1970), we focus on axisymmetric motions only and we assume that $\mathbf{u}$ is a function of s alone. Given (3) and (5), we see that the only non-zero component is the azimuthal one, so that

$$\mathbf{u} = u_\phi(s,t)\mathbf{e}_\phi. \tag{7}$$

We define the geostrophic average of the generic field $F(s,\phi,z)$ through the averaging over the surfaces Σ_c of the geostrophic cylinders, having distance s from the rotation axis and height $2H = 2\sqrt{r_c^2 - s^2}$. We indicate this operation by angle brackets and we calculate it as follows:

$$\begin{aligned}\langle F\rangle(s) &= \frac{1}{\Sigma_c}\int_{\Sigma_c} F(s,\phi,z)d\Sigma \\ &= \frac{1}{4\pi s H}\int_0^{2\pi}\int_{-H}^{H} F(s,\phi,z)s\, d\phi\, dz.\end{aligned} \tag{8}$$

Introducing the azimuthal average

$$\overline{F}(s,z) = \frac{1}{2\pi}\int_0^{2\pi} F(s,\phi,z)s\, d\phi \tag{9}$$

the geostrophic average can be written in the following compact form:

$$\langle F\rangle(s) = \frac{1}{2H}\int_{-H}^{H}\overline{F}(s,z)\, dz. \tag{10}$$

By taking the geostrophic average of the azimuthal component of the linearised Navier–Stokes eq. (1) we can derive an evolution equation for $u_\phi(s)$. Note that in the linearised equations the advection term $\rho(\mathbf{u}\cdot\nabla)\mathbf{u}$ is neglected, it being of second order in the perturbation field. If we also neglect viscosity, magnetic diffusion and coupling between the liquid core and the mantle we obtain an ideal equation that has been named the canonical torsional wave equation in Roberts & Aurnou (2012):

$$\rho s\frac{\partial u_\phi}{\partial t} = \frac{1}{2\mu_0 H s}\frac{\partial}{\partial s}(2Hs^2 c) \tag{11}$$

where $c = \langle B_{s0}B'_\phi\rangle$ satisfies the following evolution equation:

$$\frac{\partial c}{\partial t} = s\langle B_{s0}^2\rangle\frac{\partial}{\partial s}\left(\frac{u_\phi}{s}\right). \tag{12}$$

Note that even assuming that the mantle conductivity is zero, implying that the magnetic field in the mantle is a potential field, the matching with the field within the core introduces a non-local coupling between the geostrophic cylinders. This extra term adds complications that we want to avoid in this study, and therefore we neglect it. We simply note that this non-local coupling is removed for axisymmetric background fields. Its importance is thought to be negligible compared to the local coupling between the cylinders, except possibly near the equator. The reader is referred to Jault & Légaut (2005) and Roberts & Aurnou (2012) for a complete discussion about the neglected terms. By introducing the angular velocity of the geostrophic cylinders $\zeta(s,t) = u_\phi(s,t)s^{-1}$ and by combining (11) and (12) we obtain a single equation for $\zeta(s,t)$:

$$m\frac{\partial^2\zeta}{\partial t^2} = \frac{\partial}{\partial s}\left[mV_A^2\frac{\partial\zeta}{\partial s}\right] \tag{13}$$

where $m = s^3 H$ and $V_A^2 = \langle B_{s0}^2\rangle\mu_0^{-1}\rho^{-1}$ is the Alfvén velocity for the torsional waves. As it describes axisymmetric oscillations, the equation's domain of validity is $0 \le s \le r_c$, $s = 0$ being the rotation axis and $s = r_c$ the equator. An inspection of the form of m reveals that the boundary points are singular points of eq. (13). We will show in the next sections that, with an appropriate choice of the background field and of the boundary conditions, these singularities are integrable and it is numerically feasible to solve (13) over the whole domain. It is common practice (see e.g. Jault & Légaut 2005; Cox *et al.* 2014) to complement (13) with the following boundary conditions:

$$\zeta'|_{s=0} = 0 \tag{14}$$

$$\zeta'|_{s=r_c} = 0 \tag{15}$$

where the prime denotes a derivative with respect to the variable s. The first of these boundary conditions comes from regularity conditions that the field u_ϕ has to satisfy at the rotation axis (Lewis & Bellan 1990). The boundary condition at $s = r_c$ can be derived from the insulating boundary conditions (6) and the diffusion-free induction eq. (2) (Jault & Finlay 2015). These conditions are, at $s = r_c$:

$$\mu_0\frac{\partial J_s}{\partial t} = -s\frac{\partial B_s}{\partial z}\frac{\partial\zeta}{\partial s} = 0 \tag{16}$$

$$\frac{\partial\zeta}{\partial s}\overline{B_s} = 0. \tag{17}$$

The relevant geophysical case in which these conditions are derived is that of viscosity being much smaller than the magnetic diffusivity, or equivalently small magnetic Prandtl number: $Pm = \nu\eta^{-1} \ll 1$. The boundary condition on the velocity field is then adjusted across a small boundary layer over which the magnetic field is not changing. If we assume $B_s|_{s=r_c} \neq 0$ then we need the boundary condition (15). But in the special case $B_s|_{s=r_c} = 0$ then (16) and (17) are automatically satisfied. We are then left with imposing the regularity of ζ at the origin via (14).

We non-dimensionalise eqs (13)–(15) taking r_c as the characteristic length scale and scaling the time by the total traveltime Δt defined by the Alfvén velocity $V_A(s)$:

$$\Delta t = \int_0^{r_c}\frac{ds}{V_A}. \tag{18}$$

The total traveltime Δt is therefore the time taken by a high-frequency disturbance ζ to travel from the rotation axis to the equator in the Alfvén velocity field $V_A(s)$, as in the ray-theory approximation, see, for example, Chapman (2004). This point is clarified in Section 5, where we make use of the WKBJ approximation and integrals of the form (18) define the spatial dependence of high-frequency disturbances ζ.

The traveltime Δt and the size of the core r_c are used to non-dimensionalise the wave eq. (13). If we introduce the non-dimensional time $t^* = t/\Delta t$ and spatial coordinate $s^* = s/r_c$, so that $0 \le s^* \le 1$, we can write:

$$m^*\frac{\partial^2\zeta^*}{\partial t^{*2}} = \frac{\partial}{\partial s^*}\left[m^* V_A^{*2}\frac{\partial\zeta^*}{\partial s^*}\right] \tag{19}$$

where $m^* = s^{*2}H^*$, $H^* = \sqrt{1-s^{*2}}$, $V_A^* = V_A\Delta t/r_c$ and $\zeta^* = \zeta\Delta t^2/r_c$. In what follows we make use of non-dimensional variables and equations dropping the * for simplicity.

3 NORMAL MODES

The angular velocity $\zeta(s, t)$ can be expressed as a superposition of normal modes $\zeta_n(s)$, each of which satisfies the boundary conditions (14), (16), (17) and oscillates with eigenfrequency ω_n, so that:

$$\zeta(s,t) = \sum_{n\geq 0} c_n \zeta_n(s) \exp[-\mathrm{i}\omega_n t] \tag{20}$$

where c_n are coefficients set by the initial condition $\zeta_0(s) = \zeta(s, 0)$. Eigenmodes and eigenfrequencies can be formed by inserting this expansion in the wave eq. (19). The resulting normal mode equation and associated boundary conditions read, in non-dimensional form:

$$-m\omega_n^2 \zeta_n = \frac{d}{ds}\left[m V_A^2 \frac{d\zeta_n}{ds} \right] \tag{21}$$

$$\begin{aligned} &\zeta_n'|_{s=0} = 0 \\ &\zeta_n' \overline{B_{s0}}|_{s=1} = 0. \end{aligned} \tag{22}$$

This is a well-posed eigenvalue problem in Sturm–Liouville form and it is possible to determine a complete set of eigenmodes $\zeta_n(s)$ that is orthogonal with respect to the scalar product defined by the weight function $m(s)$:

$$\int_0^1 m(s)\zeta_n(s)\zeta_k(s)\, ds = ||\zeta_n||^2 \delta_{n,k}. \tag{23}$$

Here $\delta_{n,k}$ is the Kronecker symbol, equal to 1 if $n = k$ and zero otherwise and $||\zeta_n||^2$ is the squared norm of the nth mode. The solutions to (21) strongly depend on the field V_A^2. The Alfvén velocity, being calculated from the magnetic component B_{s0}, has to satisfy the appropriate regularity conditions at the rotation axis. In particular, following Lewis & Bellan (1990), V_A^2 (and therefore V_A) has to be expressed as a polynomial in s^2 close to the rotation axis:

$$V_A^2 = a_0 + a_1 s^2 + a_2 s^4 + \cdots = \sum_{i\geq 0} a_i s^{2i}. \tag{24}$$

Here a_i are the polynomial coefficients that determine the shape of V_A^2 as s tends to zero. This means that the first derivative of V_A has to vanish at $s = 0$ for any physically acceptable Alfvén velocity profile. Furthermore, it has been shown in Roberts & Aurnou (2012) that in order for the solutions to (21) to satisfy the first of the conditions (22), V_A^2 needs to be non-zero at $s = 0$.

Concerning the behaviour at the equator, it can be shown that the normal mode eq. (21) has a singular point in $s = 1$ (see Arfken *et al.* 2011, chap. 7) for any choice of V_A. However the singularity is integrable for $V_A|_{s=1} \neq 0$. Assuming that the Alfvén velocity goes to zero as $V_A = (1 - s)^\nu$ it can be shown that for $\nu \leq 1$ the equation is still integrable but for $\nu > 1$ the singularity becomes non-integrable and in general a solution does not exist. In terms of wave propagation we can also see that for $\nu \geq 1$ the integrand defining the traveltime (18) is non-integrable as s tends to 1, so that the traveltime becomes singular and a wave travelling towards the equator never reaches it. Therefore, any vanishing Alfvén velocity profile has to satisfy $\nu < 1$.

Once a valid Alfvén velocity profile is chosen, it is easy to solve the one-dimensional normal mode problem numerically. But is it possible to find analytical solutions in terms of known special functions? For the case

$$V_A = V_{A,\mathrm{const}} = 1, \tag{25}$$

Roberts & Aurnou (2012) report an analytical solution in terms of angular oblate spheroidal wave functions. We solved the normal mode eq. (21) numerically using the finite-element method software COMSOL Multiphysics for the case of constant Alfvén velocity (25). The result for the modes from $n = 1$ to $n = 6$ are shown in Fig. 1(a). Both eigenmodes and eigenfrequencies are in agreement with the solution proposed by Roberts & Aurnou (2012) and with the solution plotted in figure A1 of Mound & Buffett (2007).

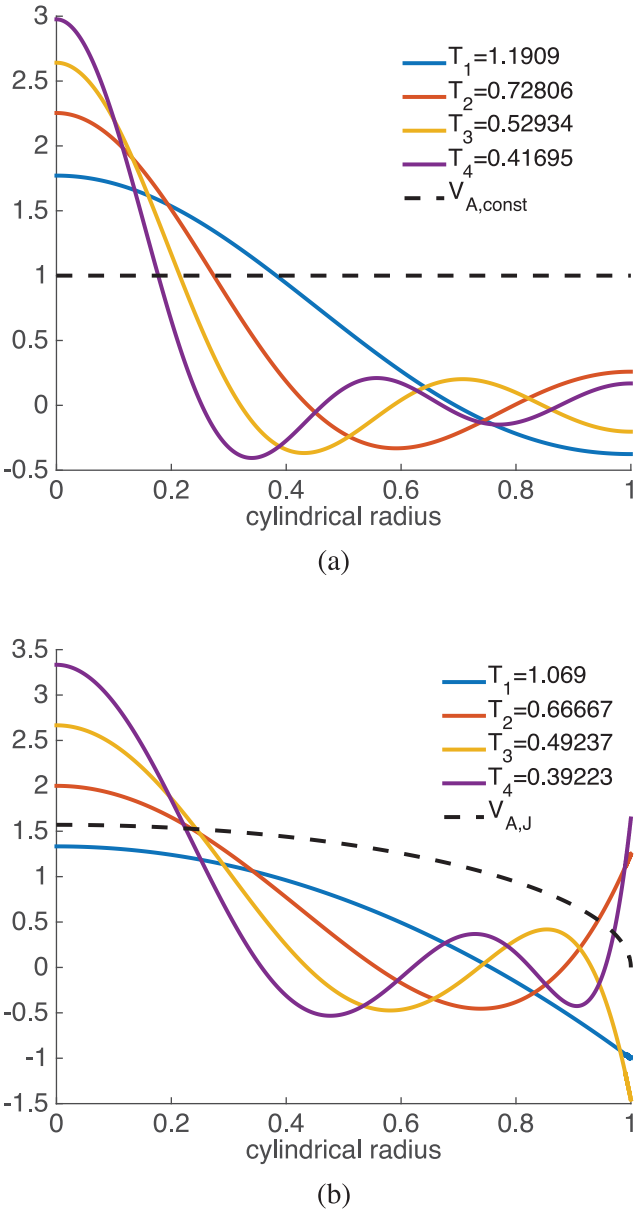

Figure 1. Numerically calculated eigenmodes and eigenperiods $T_n = 2\pi\omega_n^{-1}$ (for $1 \leq n \leq 6$) for the torsional wave normal mode eq. (21) for (a) the constant Alfvén velocity profile $V_{A,\mathrm{const}} = 1$ and (b) the Jacobi Alfvén velocity profile $V_{A,J} = \pi/2\sqrt{(1 - s^2)}$, shown in both plots as a dashed black line.

It is possible to find another solution in terms of the Jacobi polynomials. If the Alfvén velocity has the form

$$V_A = V_{A,J} = \frac{\pi}{2}\sqrt{1 - s^2} \tag{26}$$

eigenmodes and eigenfrequencies are

$$\begin{aligned} &\zeta_n(s) = P_n^{(1/2,1)}(2s^2 - 1) \\ &\omega_n = \pi\sqrt{n\,(n + 5/2)} \end{aligned} \tag{27}$$

where $P_n^{(\alpha,\beta)}$ are the Jacobi polynomials of degree n and $\alpha = 1/2$, $\beta = 1$ for our solution (Olver 2010). We call (26) and (27) the Jacobi field and the Jacobi solution, respectively. Note that $V_{A,J}$ is zero at $s = 1$ and, according to the discussion in the previous section there is no condition on ζ in $s = 1$. We calculated numerical eigenmodes and eigenfrequencies for the Jacobi field (26) and we confirmed that the numerical solution (illustrated in Fig. 1b) matches the analytical one (27).

One might ask whether the Jacobi profile (26) can be realised from a realistic background magnetic field. A profile similar, but not identical, to (26) can be constructed by a superposition of a toroidal and poloidal magnetic field of low complexity. Following Li *et al.* (2010) we considered a toroidal field of fully normalised spherical harmonics $Y_l^m(\theta, \phi)$ of degree $l = 1$ and order $m = 1$ and a poloidal field of degree $l = 1$ and order $m = 0$. In a spherical coordinate system, these fields are described by the scalar potentials $\mathcal{T}(r, \theta, \phi)$ and $\mathcal{P}(r, \theta, \phi)$, respectively. For both potentials we considered the simplest radial functional structure that satisfies insulating boundary conditions at the CMB and regularity conditions at the origin (Li *et al.* 2010). We therefore set:

$$\mathcal{T} = \tilde{V}_1 r^2(1 - r^2)Y_1^1(\theta, \phi) \tag{28}$$

$$\mathcal{P} = \tilde{V}_1 10r^2(5 - 3r^2)Y_1^0(\theta, \phi) \tag{29}$$

where $\tilde{V}_1$ is a normalisation factor. The resulting background magnetic field $\mathbf{B}_1$ is

$$\mathbf{B}_1 = [\nabla \times (\mathcal{T}\mathbf{e}_r) + C\,\nabla \times \nabla \times (\mathcal{P}\mathbf{e}_r)] \tag{30}$$

where C is a free parameter. The resulting Alfvén velocity is defined by the s component B_{s1}:

$$V_1^2 = \langle B_{s1}^2 \rangle = \tilde{V}_1^2 \frac{1}{105}(1 - s^2)(4 + (35C^2 - 8)s^2 + 4s^4). \tag{31}$$

This profile vanishes at the equator for any choice of C with non-zero derivative and satisfies regularity conditions at the rotation axis, similarly to the Jacobi field (26). For $C = \sqrt{8/35}$ we obtain the simple form

$$V_1^2 = \tilde{V}_1^2 \frac{4}{105}(1 - s^2)(1 + s^4). \tag{32}$$

In Fig. 2 we compare the root mean square value of the background magnetic field $B_{\rm rms} = \sqrt{\langle B_{s0}^2 \rangle}$ defined by the Jacobi field (26) with previous estimates from detection of torsional waves from Gillet *et al.* (2010, 2015). The field of Gillet *et al.* (2010) (the red curve in the plot) is calculated from the formula given in Canet *et al.* (2014) that gives a lower bound to the intensity of the field B_s:

$$V_A = C_g \left(\frac{3}{2} \cos[\pi(\alpha_1 + \alpha_2 s)] + 2 \right). \tag{33}$$

Here $\alpha_1 = 3/2$, $\alpha_2 = 1/0.38$ and C_g is a constant used to tune the intensity magnitude of the profile. In Fig. 2 we also show $B_{\rm rms}$ for the toroidal–poloidal field (30) with $C = \sqrt{8/35}$. To ease the comparison we normalised the Jacobi field (in black) and the field from Gillet *et al.* (2010) (in red) parametrised as in eq. (32) in Canet *et al.* (2014), so that it would give a traveltime from the tangent cylinder ($s = 0.35\,r_c$, the location of which is marked by the black dashed line) to the equator ($s = r_c$) of 6 yr. The result is in agreement with the lower bound given in Gillet *et al.* (2010) for the rms intensity of B_s in the outer core. The blue lines are direct estimates of the intensity in the interior and equatorial region of the core taken from Gillet *et al.* (2015). The four fields are qualitatively

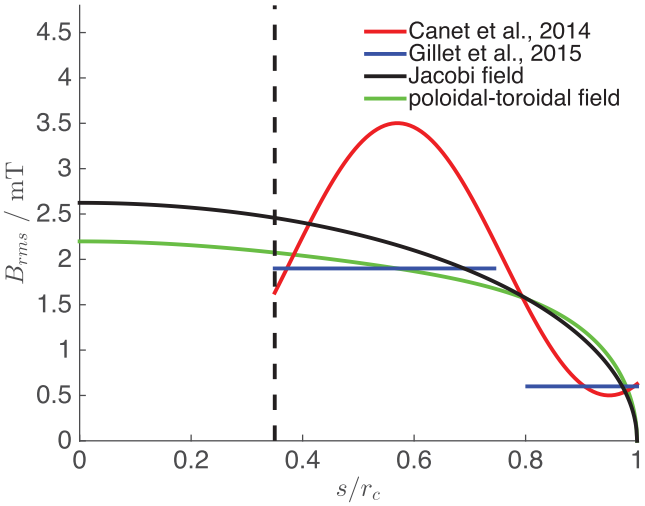

Figure 2. Comparison of the geostrophic averaged intensity of the cylindrical radial field B_s defined by the Jacobi field, $V_A = (\pi/2)\sqrt{1 - s^2}$ (black line) used in this study with intensities from previous studies inferred from torsional wave detection studies (red and blue lines). The red line is proportional to $V_A = (3/2)\cos[\pi(3/2 + s/0.38)] + 2$, which is a non-dimensional representation proposed in Canet *et al.* (2014) for the results of Gillet *et al.* (2010). Also shown is a realisation of a field (green line) obtained with a combination of toroidal and poloidal field that is qualitatively similar to the Jacobi field (see eq. 32). The black, red and green profiles are obtained by multiplying the respective non-dimensional fields by a factor that makes the traveltime of torsional waves from the tangent cylinders to the equator equal to 6 yr. The horizontal axis is the distance from the rotation axis measured on the equatorial plane in units of core radius. The vertical dashed line marks the position of the tangent cylinder.

in agreement with regard to the intensity being greater in the bulk of the core than towards the equator, in which region observational studies show slow propagation of torsional waves.

4 FORWARD MODELLING

Following the approach of Cox *et al.* (2014), we simulate the evolution of torsional waves forward in time according to (19). We choose an initial condition ζ_0 that is a sharp Gaussian pulse centred on $s_0 = 0.5$ that satisfies the boundary conditions (14) and (15):

$$\zeta_0(s) = s^2(1 - s)^2 \exp\left[-\frac{(s - s_0)^2}{\sigma^2} \right] \tag{34}$$

where σ defines the width of the pulse. For $\sigma = 0.1$, Cox *et al.* (2014) showed that already after two consecutive reflections, the initial shape is consistently smeared and hard to distinguish as the energy initially focused in the pulse is spread all over the domain. In this paper, we are interested in having a clear signal for at least two consecutive reflections so that we can easily distinguish the incident and reflected phase at both boundaries and we found that $\sigma = 0.05$ is a satisfactory choice.

The time integration of (19) with the initial condition $\sigma = 0.05$ is shown in Fig. 3 for the constant Alfvén velocity profile $V_A = V_{A,\,\rm const} = 1$ and in Fig. 4 for the Jacobi profile $V_A = V_{A,J}$. We performed a numerical simulation implementing a low-order backward differentiation formula (BDF) scheme with 500 elements in COMSOL. The time integration algorithm is chosen for its fast damping action of high frequencies. The same results are obtained by projecting the initial condition on the set of normal

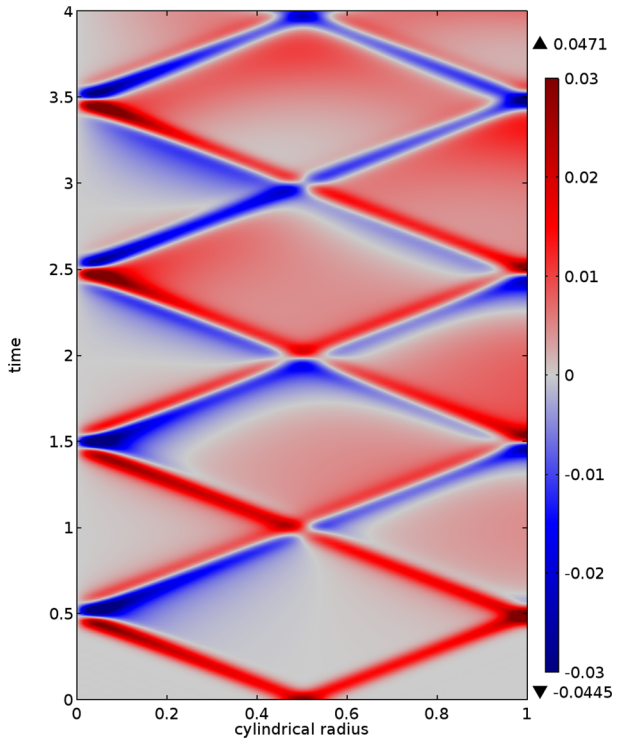

(a)

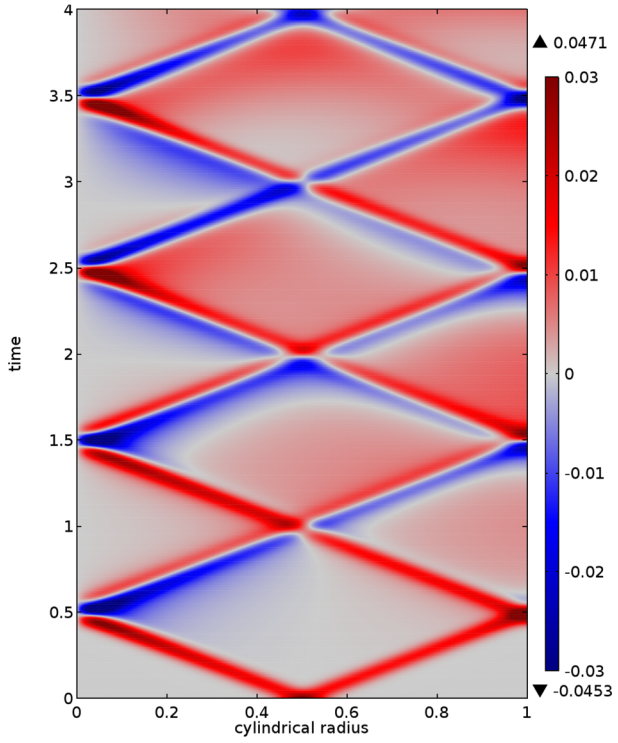

(b)

Figure 3. Time evolution of the azimuthal velocity $u_\phi = s\zeta$ from the initial pulse ζ_0 centred on $s = 0.5$ and with $\sigma = 0.05$, according to the torsional wave eq. (13) with constant Alfvén velocity profile. Panel (a) shows the solution obtained evolving in time the normal mode decomposition of the initial condition. Panel (b) shows the numerical simulation of the torsional wave equation obtained with COMSOL Multiphysics.

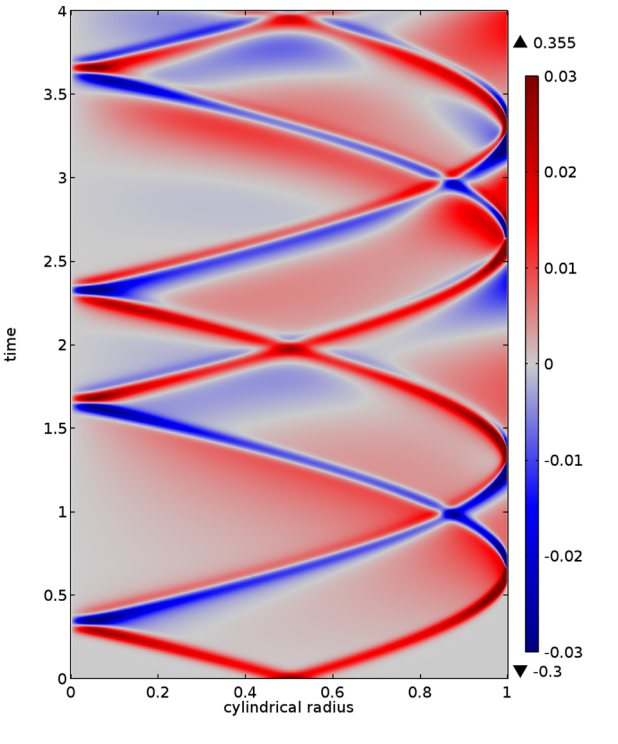

(a)

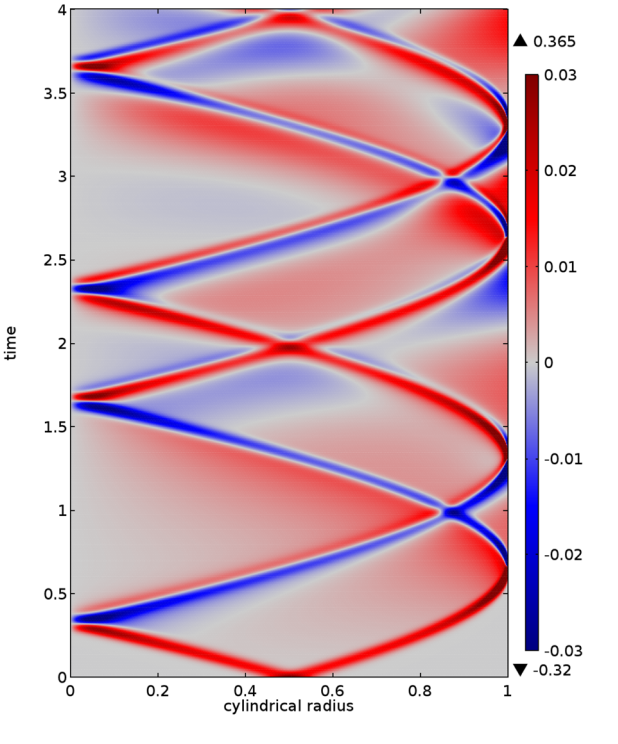

(b)

Figure 4. Time evolution of the azimuthal velocity $u_\phi = s\zeta$ from the initial pulse ζ_0 centred on $s = 0.5$ and with $\sigma = 0.05$, according to the torsional wave eq. (13) with the Jacobi Alfvén velocity profile, $V_A = (\pi/2)\sqrt{1 - s^2}$. Panel (a) shows the solution obtained evolving in time the normal mode decomposition of the initial condition. Panel (b) shows the numerical simulation of the torsional wave equation obtained with COMSOL Multiphysics.

modes illustrated in the previous section and evolving them in time according to (20). For the case of the constant Alfvén velocity we use the normal modes and eigenfrequencies numerically calculated with COMSOL. The projection of the initial condition on the normal modes according to the scalar product (23) determines the coefficients c_n. The integrals have been calculated via the trapezoidal rule. Note that we also have to take into account the mode $n = 0$ having constant value all over the domain and $\omega_0 = 0$: this mode is what in Roberts & Aurnou (2012) is called the exceptional mode. We find that the initial condition is well reconstructed by the first 39 modes (i.e. up to $n = 38$). Substituting the appropriate values for c_n and ω_n in (20) we obtain the solution that is plotted in Fig. 3(a) which is visually identical to the numerical simulation performed with COMSOL shown in Fig. 3(b). The same procedure is performed for the Jacobi field and since for this case we have a fully analytical solution, we calculate the eigenmodes and eigenfrequencies according to (27). To obtain the coefficients c_n we calculate the scalar products (23) via Gauss–Jacobi quadrature. In this case, the modes $n > 50$ contribute negligibly to the solution. For the Jacobi field case, the normal mode solution is plotted in Fig. 4(a) and the COMSOL solution is shown in Fig. 4(b).

Fig. 3 is analogous to figure 3 in Cox *et al.* (2014), only the initial pulse is sharper and the time evolution cleaner. We see that the pulses, initially focused on $s = s_0$ get split in two phases travelling in opposite directions with the same Alfvén velocity equal to $V_{A,\,\mathrm{const}}$. It is clear that the spherical geometry alters the intensity of the pulse as it travels across the core. The geometrical effects are due to the spatially varying factor $m(s)$ in eq. (19) and are analysed in Cox *et al.* (2014).

The reflection at the rotation axis looks similar in both cases because the Alfvén velocity field needs to tend to a constant as s tends to 0. This behaviour is also observable when we compare the first reflection at the rotation axis in Figs 3 and 4. The first reflection at $s = 1$ behaves differently in the two cases. For the constant background magnetic field case the reflection is dominated by a positive phase while in the Jacobi velocity field the effect of the reflection at the equator appears to be mainly to fully invert the polarity of the incoming wave. Numerical results with other Alfvén velocity profiles show that the wave reflected at $s = 1$ (when present) is always composed of a positive phase followed by a negative one and, as V_A gets smaller and smaller at $s = 1$ compared to its value at $s = 0$, the phase carrying the main part of the angular momentum slowly becomes the negative one.

In order to address the case where V_A is small but finite at the outer boundary, in Fig. 5 we show the propagation of torsional waves evolved in the Alfvén velocity profile

$$V_A = V_{A,nz} = 1.317\sqrt{1 - 0.9s^2}. \tag{35}$$

This profile represents a more realistic situation in which the Alfvén velocity field decreases towards the equator without vanishing. We evolved the same initial condition as in the other cases. As expected the reflection at the rotation axis is analogous to both Figs 3 and 4. At the equator, the first reflection preserves the positive phase as the dominant one, as in the case of the constant field. We observe, however, the increased amplitude of the trailing negative phase compared to Fig. 3. Subsequent reflections also are similar in Figs 5 and 3, and we will return to them at the end of the next section.

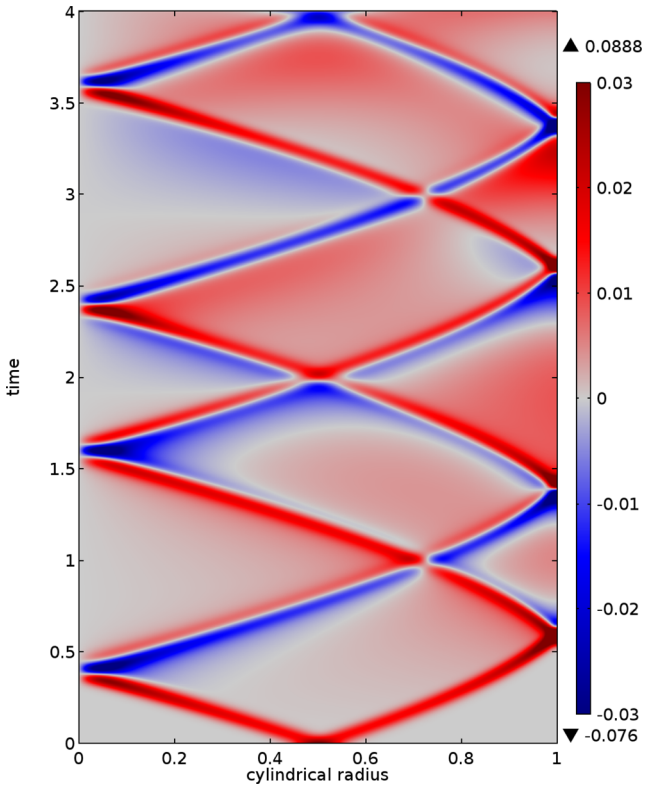

Figure 5. Time evolution of the azimuthal velocity $u_\phi = s\zeta$ from the initial pulse ζ_0 centred on $s = 0.5$ and with $\sigma = 0.05$, according to the torsional wave eq. (13) with Alfvén velocity profile (35), $V_A = 1.317\sqrt{1 - 0.9s^2}$. The picture shows the numerical solution obtained with COMSOL Multiphysics.

5 WKBJ APPROXIMATION AND REFLECTION COEFFICIENTS

Following Bender & Orszag (1999, chap. 10) the WKBJ ansatz is

$$\zeta(s) \simeq \exp\left[\frac{1}{\delta}\sum_{i\geq 0}\delta^i S_i(s)\right] = \exp\left[\frac{1}{\delta}S_0(s) + S_1(s) + \delta S_2(s) + \cdots\right] \tag{36}$$

with δ a small parameter and $S_i \in \mathbb{C}$. This approximation is widely applied in seismology (Chapman 2004), and it is generally valid when the heterogeneities of the medium are at a much larger spatial scale than the oscillations of the function $\zeta(s)$. By valid we mean that the series (36) converges to the non-approximated solution as $\delta \to 0$. In our case we expect the WKBJ approximation to be valid away from the boundaries and for high-frequency oscillations. Formally, as $\delta \to 0$, the conditions for the validity of the ansatz (36) are expressed by the requirement that:

$$\delta|S_{i+1}(s)| \ll |S_i(s)|. \tag{37}$$

For any term $i \geq 0$. These conditions tell us that each term is less important than the preceding one. For more on the validity conditions of the series (36) the reader is referred to Bender & Orszag (1999) and to Appendix A. We consider a wave packet that is expressed as

$$\zeta(s,t) = \zeta(s)\exp[-\mathrm{i}\omega t] \tag{38}$$

where $\zeta(s)$ is expressed by the WKBJ expansion truncated at order $n = 1$:

$$\zeta(s) = \exp\left[\frac{1}{\delta}S_0(s) + S_1(s)\right]. \tag{39}$$

The evolution eq. (19) becomes

$$-m\omega^2\zeta = \frac{d}{ds}\left[mV_A^2\frac{d\zeta}{ds}\right] \tag{40}$$

where ζ is an approximation to the normal modes. By inserting (39) in (40) and after some algebra (see the detailed calculations in Appendix A) we find that $\delta = \omega^{-1}$ and that:

$$\omega S_0(s) = \pm i\omega\int\frac{ds}{V_A(s)} = \pm i\omega\tau(s) \tag{41}$$

$$S_1(s) = \ln\sqrt{\frac{1}{m(s)V_A(s)}} \tag{42}$$

so that

$$\zeta(s) = \sqrt{\frac{1}{m(s)V_A(s)}}\{A_+\exp[+i\omega\tau(s)] + A_-\exp[-i\omega\tau(s)]\} \tag{43}$$

or

$$\zeta(s) = \sqrt{\frac{1}{m(s)V_A(s)}}\{A_c\cos[\omega\tau(s)] + A_s\sin[\omega\tau(s)]\} \tag{44}$$

where A_+, A_-, A_c and A_s are coefficients to be determined (see below) and $\tau(s)$ is a traveltime analogous to (18) but defined by an indefinite integral, thus requiring the introduction of an integration constant to be defined (see below). As the approximation cannot be used at the boundaries, in general we need to calculate the solutions to the approximated torsional wave equation valid near $s = 0$ and $s = 1$ that satisfy the boundary conditions. We divide the domain $0 \le s \le 1$ in three subdomains that we call *I*, *II* and *III* defined, respectively, for $0 \le s \le s_1$, $s_1 \le s \le s_2$ and $s_2 \le s \le 1$. In these three regions, the approximate solutions are called $\zeta_I(s)$, $\zeta_{II}(s)$ and $\zeta_{III}(s)$. The exact locations of s_1 and s_2 are not specified but we always assume that in regions *I* and *III* we have $s \ll 1$ and $1 - s \ll 1$, respectively. In the subdomain *II*, the solution is given by the WKBJ approximation (43) or (44). The coefficients A_+, A_- (or A_c, A_s) and the eigenfrequencies are found by matching these three solutions on the overlapping regions of validity around s_1 and s_2. This procedure (called asymptotic matching) is outlined and illustrated in Bender & Orszag (1999).

5.1 Normal modes WKBJ approximation

Here we show how the WKBJ approximation can be applied to approximate the normal modes for the case of the Jacobi solution. By inserting (26) in (44) we obtain the following WKBJ approximation:

$$\zeta_{II}(s) = \sqrt{\frac{2}{\pi}}\frac{1}{s^{3/2}H}\left[A_c\cos\left(2\frac{\omega}{\pi}\arcsin(s) + \omega\eta\right) + A_s\sin\left(2\frac{\omega}{\pi}\arcsin(s) + \omega\eta\right)\right] \tag{45}$$

where η is an integration constant. The differential equations for the boundary solutions ζ_I and ζ_{III} are, respectively:

$$\omega^2 s^3\zeta_I(s) + \frac{d}{ds}\left[\frac{s^3}{4}\frac{d\zeta_I(s)}{ds}\right] = 0 \tag{46}$$

and, upon the substitution $z = 1 - s$,

$$\omega^2 z^{1/2}\zeta_{III}(z) + \frac{d}{dz}\left[\frac{z^{3/2}}{2}\frac{d\zeta_{III}(z)}{dz}\right] = 0 \tag{47}$$

The solutions to these equations are:

$$\zeta_I(s) = \frac{A_I}{s}J_1\left(2\frac{\omega}{\pi}s\right) \tag{48}$$

$$\zeta_{III}(s) = \frac{A_{III}\pi}{2\omega H}\sin\left(2\frac{\omega}{\pi}H\right). \tag{49}$$

Here, J_1 is the Bessel function of first kind and first order and A_I and A_{III} are constants to be determined via the matching technique. Note that the boundary solution (48) obtained in the region where we can assume H to be a constant, is the normal mode solution in a cylindrical domain and has been used in Mound & Buffett (2007) and Cox *et al.* (2014) to derive approximated solutions for propagation and reflection of torsional waves in the sphere.

To match solutions we require that in the overlapping regions around s_1 and s_2 the boundary solutions and the WKBJ approximation have the same functional form. This is achieved by approximating (45) for $s_1 \ll 1$ and $1 - s_2 \ll 1$, which is a similar requirement that led to the solutions ζ_I and ζ_{III}, and by approximating the solution ζ_I for large values of its arguments. This leads us to the asymptotic expansion of the Bessel function J_1, valid for $2\omega s \gg 0$ (see e.g. Abramowitz & Stegun 1965, eq. 9.2.1):

$$\zeta_I(s) \simeq \frac{A_I}{s^{3/2}}\sqrt{\frac{\pi}{\pi\omega}}\cos\left(2\frac{\omega}{\pi}s - \frac{3}{4}\pi\right). \tag{50}$$

Note that, since we expect this approximated solution to be valid for high frequencies, the limit $2\omega s$ does not contradict the hypothesis $s_1 \ll 1$, but conversely defines the overlapping region where both ζ_{II} and ζ_I can be considered a valid approximation to the true solution. In this region $\arcsin(s) \simeq s$ and $s^{3/2}H \simeq s^{3/2}$ so that the two approximations have the same functional form. Therefore the matching requires:

$$\omega\eta = -\frac{3}{4}\pi\,; \quad A_s = 0\,; \quad A_c = A_I\frac{\pi}{\sqrt{2\pi\omega}}. \tag{51}$$

In the overlapping region around s_2 we have $s^{3/2}H \simeq H$ and $\arcsin(s) \simeq \pi/2 - H$ and the matching with (49) leads us to:

$$A_{III} = 2(-1)^n A_I\sqrt{\frac{\omega}{\pi}}\,; \quad \frac{\omega}{\pi} = \frac{5}{4} + n. \tag{52}$$

We did not approximate the boundary solution ζ_{III} on the overlapping region around s_2 as the approximated ζ_{II} for $1 - s_2 \ll 1$ and ζ_{III} already had the same functional form and the matching was already possible. The second of the conditions (52) defines the WKBJ approximation to the normal modes

$$\hat{\omega}_n = \pi\left(n + \frac{5}{4}\right) \tag{53}$$

and by inserting (51) and (52) in (45), (48) and (49) we obtain the WKBJ approximation to the normal mode solution:

$$\zeta_I(s) = \frac{A_I}{s}J_1\left(2\frac{\hat{\omega}_n}{\pi}s\right) \tag{54}$$

$$\zeta_{II}(s) = A_I\sqrt{\frac{\pi}{\pi\hat{\omega}_n}}\frac{1}{s^{3/2}H}\cos\left(2\frac{\hat{\omega}_n}{\pi}\arcsin(s) - \frac{3}{4}\pi\right) \tag{55}$$

$$\zeta_{III}(s) = (-1)^n\frac{A_I}{H}\sqrt{\frac{\pi}{\pi\hat{\omega}_n}}\sin\left(2\frac{\hat{\omega}_n}{\pi}H\right) \tag{56}$$

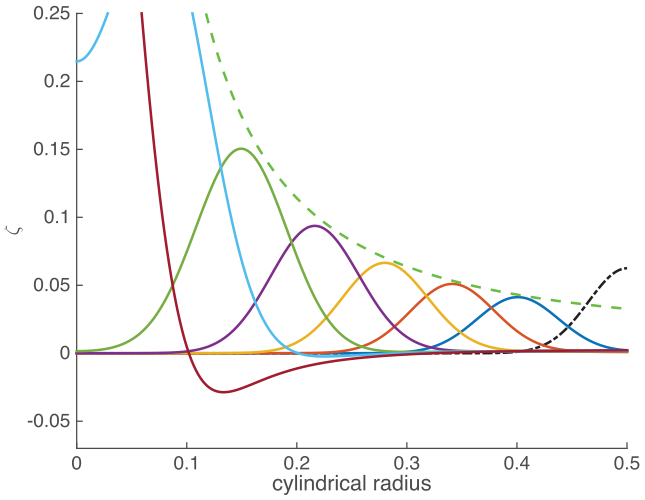

(a)

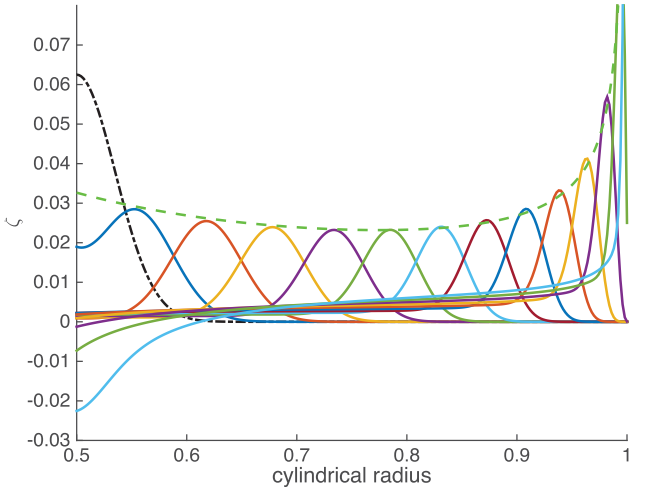

(b)

Figure 6. Successive snapshots of time evolution (coloured continuous lines) from the initial condition showed by the black dot-dashed line before the occurrence of the first reflection with the Jacobi Alfvén velocity profile. The dashed green line is the s-varying amplitude of the WKBJ solution. Panel (a) shows the time evolution for $0 < s < 0.5$ and for $0 < t < \pi/3$ and panel (b) shows the time evolution for $0.5 < s < 1$ and for $0 < t < 2\pi/3$.

where A_I is a free parameter that sets the amplitude of the oscillations.

In Fig. 6 we show how the modulation factor of the WKBJ solution defined by $\exp(S_1(s))$ reproduces well the envelope of the time-dependent solution for the Jacobi field, shown in Fig. 6.

In Fig. 7 we compare the true eigenfrequencies (27) and the WKBJ approximation (53) for n between 1 and 20. As the WKBJ solution is an asymptotically valid approximation for high frequencies, we note that the relative error approaches zero as n increases. Indeed (53) is exactly the large n approximation to the true solution. We also note that the approximated solution predicts the correct frequencies with an error that is always less than 10 per cent, for $n \geq 2$. In Fig. 8, we compare the WKBJ eigenmodes with the Jacobi solution $A_I = 1$. In the first row, we show the first and the second term in the WKBJ expansion, $S_0(s)$ and $S_1(s)$. From the figure we can confirm that $\omega S_0(s) \gg S_1(s)$ is satisfied in the interior of the

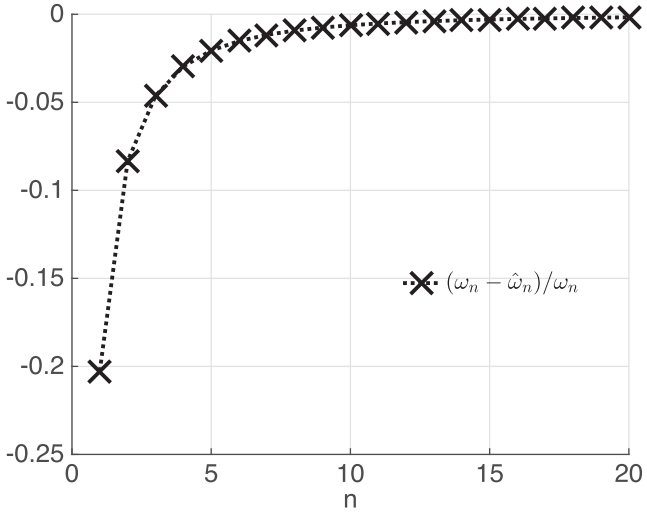

Figure 7. Relative error between the true Jacobi eigenfrequencies ω_n and the WKBJ approximations $\hat{\omega}_n$.

domain, thus validating the WKBJ approximation there. Also note that the region of validity increases as we consider modes with larger frequencies. We use these plots to define *a posteriori* the points s_1 and s_2 as the two points for which $\omega S_0(s) = S_1(s)$. From the geometry of the curves, we see that there are always two points in which the two curves intersect but although s_1 is always visible on the plot, $s = s_2$ is indistinguishable from $s = 1$, therefore we do not mark the position of the latter. We see on the second row of Fig. 8 that there is a region around $s = s_1$ for which both ζ_I and ζ_{II} are acceptable approximations to the true mode and the approximation gets better with increasing n. For $n > 3$, ζ_{III} overlaps with ζ_{II} as s approaches 1. Hence, the reason why $s = s_2$ is not visible on the plots is because ζ_{II} is a good approximation all the way to the equatorial boundary. However we needed the mathematical form of ζ_{III} to constrain the allowed frequencies.

We demonstrated that the WKBJ approximation is an efficient tool to find the solution of the torsional wave equation and we proceeded to apply this tool to the study of the propagation properties of travelling waves and their reflections at the boundaries.

5.2 Reflections and phase shifts

We first focus on the reflection at the rotation axis. According to the time evolution studies we described in Section 4 we consider a wave packet moving from the bulk of the domain towards the rotation axis approximated by the WKBJ solution (38):

$$\zeta_1(s,t) = \sqrt{\frac{2}{\pi}}\frac{1}{s^{3/2}H}\exp\left[-2\mathrm{i}\frac{\omega}{\pi}\arcsin(s) - \mathrm{i}\omega t\right]. \tag{57}$$

The wave enters the region I, crosses the rotation axis where the pseudo-reflection takes place, and starts to travel in the opposite direction, finally leaving the region I and then being described by a WKBJ approximated solution that we call $\zeta_2(s,t)$:

$$\zeta_2(s,t) = \sqrt{\frac{2}{\pi}}\frac{1}{s^{3/2}H}\exp\left[2\mathrm{i}\frac{\omega}{\pi}\arcsin(s) - \mathrm{i}\omega t + \mathrm{i}\mu_0\right]. \tag{58}$$

The reflection coefficient $R_0 = \zeta_2/\zeta_1$ at the rotation axis is described by the, possibly complex, phase shift μ_0. The phase shift is found by matching (57) and (58) with the travelling boundary solution $\zeta_I(s,t) = \zeta_I(s)\exp[-\mathrm{i}\omega t]$ in the overlapping region around s_1, in the same way as the normal modes approximation (54)–(56) is obtained. This

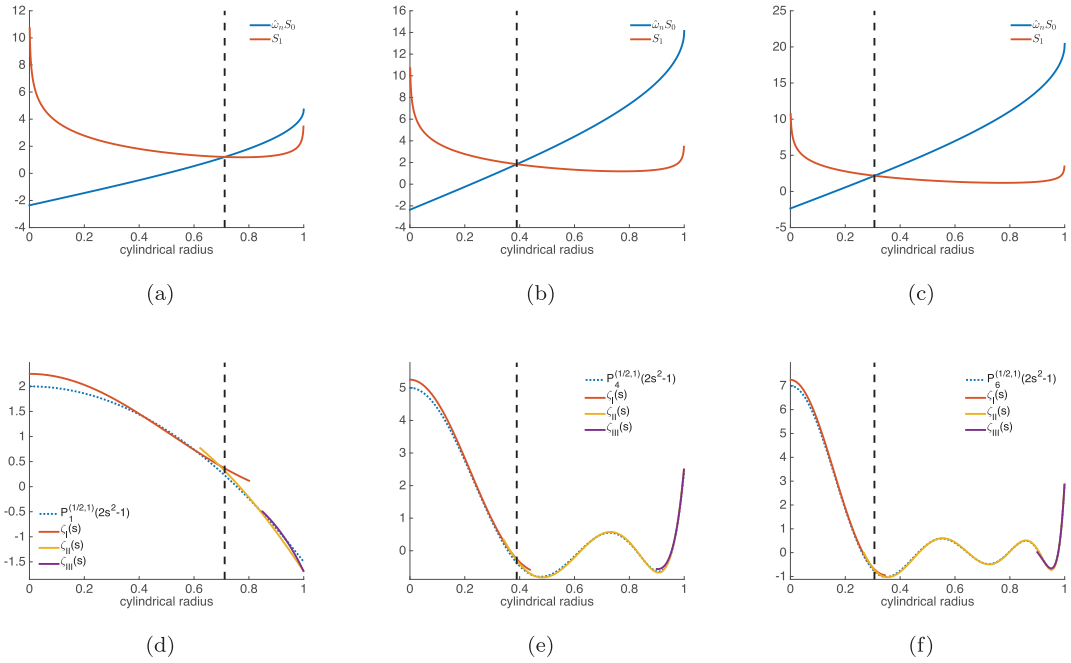

Figure 8. WKBJ approximation of the Jacobi eigenmodes. The first, second and third columns illustrate the $n = 1$, $n = 4$ and $n = 6$ eigenmodes. In the first row we compare the functions $\hat{\omega}_n S_0(s) = 2\frac{\hat{\omega}_n}{\pi}\arcsin(s) - \frac{3}{4}\pi$ in blue and $S_1 = \log\left[\sqrt{\frac{2}{\pi}}\frac{1}{s^{3/2}H}\right]$ in red. In the second row we compare the WKBJ solution (yellow) the boundary solutions (red and purple) with the non-approximated normal mode (dotted blue). The black dashed line indicates the point $s = s_1$, defined by $\hat{\omega}_n S_0(s) = S_1(s)$. The point $s = s_2$ is indistinguishable from $s = 1$ in these plots.

procedure leads us to the real and frequency independent phase shift for the reflection at the rotation axis:

$$\mu_0 = -\frac{3}{2}\pi. \tag{59}$$

This is equivalent to a phase shift of $\pi/2$ which resembles the effect of the Hilbert transform and is analogous to the one derived in Chapman (2004, section 7.2) for the passage of a seismic wave trough a caustic or an inflection point. The same conclusion was postulated for cylindrical domains in Cox *et al.* (2014) and explained by recognising that the rotation axis is a caustic for torsional waves.

The same procedure is repeated for the reflection at the equator. Here, we describe the reflection coefficient via the phase shift μ_1 and we change the propagation directions of the incident and reflected WKBJ phases (which we call ζ_1 and ζ_2, respectively):

$$\zeta_1(s,t) = \frac{\sqrt{2}}{s^{3/2}H}\exp\left[2\mathrm{i}\omega\arcsin(s) - \mathrm{i}\omega t\right] \tag{60}$$

$$\zeta_2(s,t) = \frac{\sqrt{2}}{s^{3/2}H}\exp\left[-2\mathrm{i}\omega\arcsin(s) - \mathrm{i}\omega t + \mathrm{i}\mu_1\right]. \tag{61}$$

By performing the matching with the travelling boundary solution $\zeta_{III}(s,t) = \zeta_{III}(s)\exp[-\mathrm{i}\omega t]$ we find

$$\mu_1 = 2\pi\frac{\omega}{\pi} + \pi. \tag{62}$$

At the equator the phase shift is frequency dependent.

To validate these results, we project on the normal mode solution (27) a generalised version of the initial condition (34):

$$\zeta_0(s) = s^2(s-1)^2\cos(2\pi s/\lambda)\mathrm{e}^{-\frac{(s-s_0)^2}{\sigma^2}}. \tag{63}$$

By choosing a finite value of λ we generate initial conditions that are richer in high frequencies than (34). We chose $\lambda = 0.1$ and s_0 is set to be either 0.5 or $s_0 = 0$ to study the reflection at the rotation axis and at the equator, respectively. The incident wave ζ_1 is then projected onto the Jacobi basis as well and the phase of each component is advanced by (59) or (62). The result is shown in Fig. 9. The phase shifts μ_0 and μ_1 predict well the reflected wave. We also confirm that the wave reflected at the rotation axis is approximated well by taking the Hilbert transform (and inverting its sign) of the incident wave. Incidentally, this also seems to be working well for the reflection at the equator, although the phase shift μ_1 is frequency dependent while the Hilbert transform introduces a frequency independent phase shift in each component. This coincidental agreement does not work if we were to analyse reflections in other Alfvén velocity profiles. Note that while the phase advance of each Jacobi component results in a profile that satisfies the boundary condition (14) at $s = 0$, the Hilbert transform of the incident wave does not.

So far we focused on the first reflections only (at both boundaries). Analysis of subsequent reflections reveals that a general form of the phase shifts (59) and (62) is obtained by introducing a multiplying factor $(-1)^k$ where k increases by 1 at any pseudo-reflection at the rotation axis:

$$\mu_0 = (-1)^{k+1}\frac{3}{2}\pi \tag{64}$$

$$\mu_1 = (-1)^k\, 2\pi\frac{\omega}{\pi} + \pi. \tag{65}$$

For the first reflections ($k = 0$) the relevant phase shifts are given by (59) and (62). The factor k is the equivalent of the KMAH (Keller–Maslov–Arnold–Hörmander) index used in seismology to describe the cumulative phase shift introduced by the presence of multiple caustics along the path of a seismic ray. As an example we show in Fig. 10 the third reflection on the rotation axis of the pulse evolved from the initial condition (63) with $\lambda = 0.1$ and $s_0 = 0.5$. The pulse we consider in this reflection is the one initially travelling towards the rotation axis, undergoing one reflection there and one reflection at the equator before reaching the rotation axis again. The

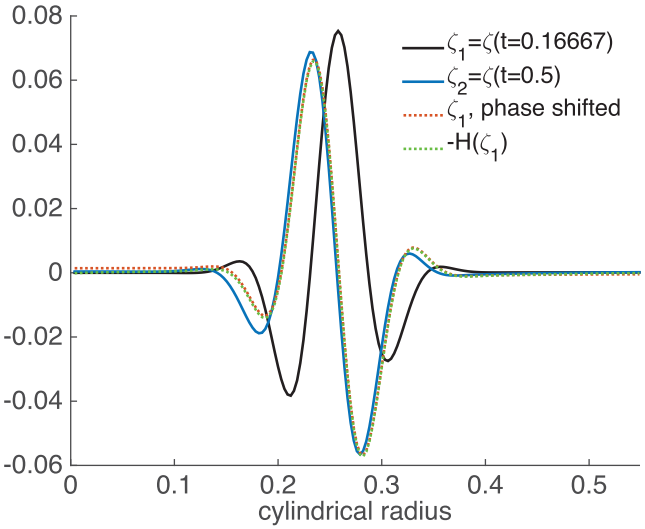

(a)

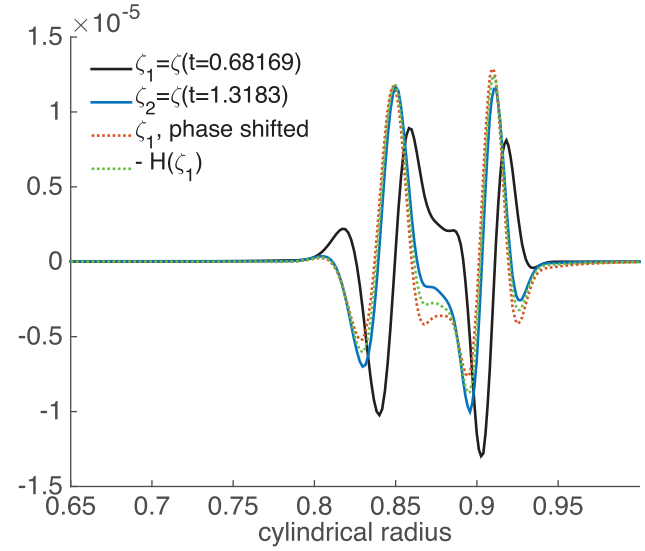

(b)

Figure 9. First reflection at (a) the rotation axis and (b) the equator for the Jacobi field. ζ_1 (black) is the incident wave and ζ_2 (blue) is the reflected wave obtained from the time evolution from an initial condition $\zeta_0(s) = s^2(s-1)^2\cos(2\pi s/\lambda)e^{-\frac{(s-s_0)^2}{\sigma^2}}$ with $\lambda = 0.1$ and (a) $s_0 = 0.5$ or (b) $s_0 = 0$. The dotted red line is obtained by projecting ζ_1 onto the Jacobi normal modes basis and advancing in time every phase according to the phase shifts (59) or (62). The green dotted line is the minus Hilbert transform of the incident wave.

reflected wave is well reproduced by introducing the phase shift (65) with $k = 1$. A similar conclusion is valid for the constant field case. Although we do not give the expressions for the reflection coefficients in this case, inspection of Fig. 3 reveals that while the first reflection at the equator has a reflection coefficient close to 1, the second and the third reflection looks more similar to -1. These are in fact reflections of pulses that crossed the rotation axis once, with a KMAH index 1. The fourth reflection is again similar to a perfect reflection as the pulse crossed the rotation axis twice and the KMAH index is 2, therefore the original reflection coefficient is retrieved.

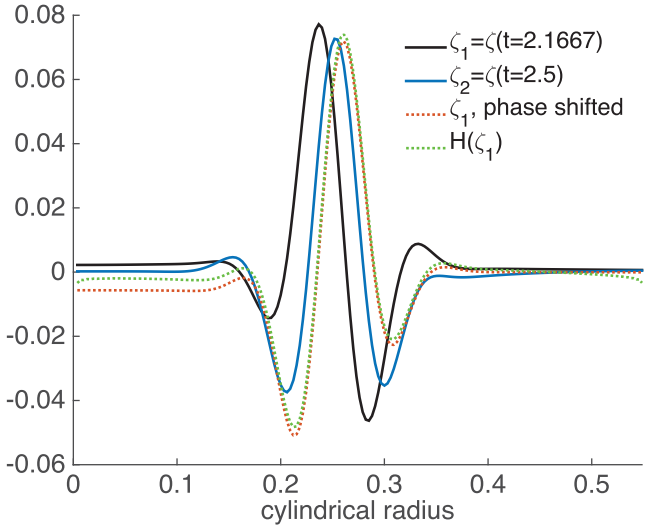

Figure 10. Third reflection at the rotation axis. The reflection time is $t = 7/3$. ζ_1 (black) is the incident wave ($t = 7/3 - 1/6$) and ζ_2 (blue) is the reflected wave ($t = 7/3 + 1/6$) obtained from the time evolution from the initial condition $\zeta_0(s) = s^2(s-1)^2\cos(2\pi s/\lambda)e^{-\frac{(s-s_0)^2}{\sigma^2}}$ for $s_0 = 0.5$, $\lambda = 0.1$ and with the Jacobi field. The dotted red line is obtained by projecting ζ_1 onto the Jacobi normal modes basis and advancing in time every phase according to the phase shifts (64) with $k = 1$. The green dotted line is the Hilbert transform of the incident wave.

6 CONCLUSIONS AND DISCUSSION

The first accomplishment of this study is the introduction of a novel closed form solution to the torsional wave eigenvalue problem, valid for the special case of a background magnetic field that vanishes at the equatorial boundary that we called the Jacobi field.

Furthermore we illustrate that waves propagating in such magnetic field are reflected at the equator differently from the case of a constant magnetic field. In the latter case qualitative inspection suggests that the reflection coefficient is close to 1, as suggested by Schaeffer *et al.* (2012) for an insulating boundary on which the flow has to satisfy stress-free boundary conditions. For the Jacobi field, however, the reflection coefficient is different. In Section 5 we propose a general method that can be used to find reflection coefficient given the Alfvén velocity profile. Applying this method to the Jacobi field we suggest that the reflection coefficient depends on the behaviour of the background magnetic field. In Schaeffer *et al.* (2012) it is shown that torsional waves propagating in the externally imposed background field $\mathbf{B}_0 = (s, 0, 2z)$ in the limit of small magnetic Prandtl number Pm, reflect at the equator with a reflection coefficient of about $R = 0.8$, while the analogous case in a linear geometry shows perfect refection ($R = 1$) for the constant field case. We did not analyse this particular magnetic field and although the limit of small Pm best describes the ideal case (see eq. 4 of Schaeffer *et al.* 2012), the results of Schaeffer and colleagues are calculated from a model that retains both viscosity and magnetic diffusion. However we can explain the reflection coefficient of $R = 0.8$ by noting that this value was calculated as the ratio of the maximum amplitudes of the incident and reflected waves at a given location. Since we showed that in general the reflection coefficient is complex, the reflected wave will be distorted with respect to the incident one, and will in general have a weaker negative phase. The main positive phase will have reduced amplitude compared to the incident wave. An accurate analysis is required to confirm this

hypothesis, as the reflection coefficient might, in general, not be a trivial function of the Alfvén velocity profile.

The reflection coefficient derived for the pseudo-reflection at the rotation axis, on the other hand, is of general character as B_s and therefore the Alfvén speed has to satisfy strict regularity conditions (as described in Section 3) and the reflection coefficient derived here is not a function of the frequency of the incident wave. Any other Alfvén velocity profile will result in the same phase shift as the boundary solution next to the rotation axis is a general one. For practical applications, we do not expect the reflected waves at the rotation axis to be an important part of the total angular momentum budget since the presence of the inner core would cause partial reflection at the tangent cylinder and little angular momentum would get inside.

Given that there are reflections at both boundaries (in particular at the equator) for valid background fields we return to the initial question: Why do torsional wave propagation patterns derived from observations not show any reflection? Our results suggest that in the ideal case there is always reflection at the boundaries, and indeed this is required by the conservation of angular momentum. Note that Gillet *et al.* (2010) found that in the time window where the waves are easily detected, they are excited at the tangent cylinder by a mechanism that is in resonance with the fundamental period (possibly due to thermochemical convection or other geodynamo fluctuations). Furthermore they allowed for finite electrical conductivity in the lower mantle, thus introducing an additional damping term in the torsional wave equation that inhibits reflection at the equator. There is thus a need to extend this study to the case of non-negligible bulk dissipation and core–mantle coupling. One first step is to reproduce the results of Schaeffer *et al.* (2012). In particular their results indicate total lack of reflection at the equatorial boundary for $Pm = 1$, that is when the kinematic viscosity ν has the same value of the magnetic diffusivity η. In this case the study suggests that all the energy transported by the wave is dissipated in the boundary layer that forms below the CMB. A geophysically more relevant study (unpublished) conducted by the same authors was aimed at studying the reflection of torsional waves in the presence of a conducting layer at the base of the mantle. It has been suggested that for realistic values of core and mantle conductivities, reflection is suppressed at the equatorial boundary. In these studies, torsional waves are simulated by use of a 3-D numerical code that can model the boundary layer effects not only at the equator but in the whole domain. On the other hand, all the effects that the CMB has on the propagation of torsional waves need to be parametrised in the 1-D model analysed in this study. Further work is necessary to extend the wave eq. (19) in order to take into account the non-ideal effects outlined above.

ACKNOWLEDGEMENTS

This work is supported by the ETH project grant number ETH-14 12-1. We thank David Al Attar (Cambridge University) and Elisabeth Canet (ETH-Zürich) for fruitful discussions and useful suggestions. We would also like to thank the reviewers, Drs Jon Mound and Dominique Jault, for their careful reading of the manuscript and useful comments which led to an improved manuscript.

REFERENCES

Abarco del Rio, R., Gambis, D. & Salstein, D.A., 2001. Interannual signals in length of day and atmospheric angular momentum, *Ann. Geophys.,* **18**(3), 347–364.

Abramowitz, M. & Stegun, I.A., 1965. *Handbook of Mathematical Functions: With Formulas, Graphs, and Mathematical Tables,* 9th edn, Dover Publications.

Alfvén, H., 1942. Existence of electromagnetic-hydrodynamic waves, *Nature,* **150**(3805), 405–406.

Arfken, G.B., Weber, H.-J. & Harris, F.E., 2011. *Mathematical Methods for Physicists: A Comprehensive Guide,* Academic Press.

Aubert, J., Labrosse, S. & Poitou, C., 2009. Modelling the palaeo-evolution of the geodynamo, *Geophys. J. Int.,* **179**(3), 1414–1428.

Bender, C.M. & Orszag, S.A., 1999. *Advanced Mathematical Methods for Scientists and Engineers I: Asymptotic Methods and Perturbation Theory,* Springer Science & Business Media.

Braginsky, S., 1970. Torsional magnetohydrodynamic vibrations in the Earth's core and variations in day length, *Geomag. Aeron.,* **10,** 1–8.

Buffett, B.A. & Mound, J.E., 2005. A Green's function for the excitation of torsional oscillations in the Earth's core, *J. geophys. Res.,* **110,** B08104, doi:10.1029/2004JB003495.

Canet, E., Finlay, C.C. & Fournier, A., 2014. Hydromagnetic quasi-geostrophic modes in rapidly rotating planetary cores, *Phys. Earth planet. Inter.,* **229,** 1–15.

Chapman, C., 2004. *Fundamentals of Seismic Wave Propagation,* Cambridge Univ. Press.

Cox, G.A., Livermore, P.W. & Mound, J.E., 2014. Forward models of torsional waves: dispersion and geometric effects, *Geophys. J. Int.,* **196**(3), 1311–1329.

Gillet, N., Jault, D., Canet, E. & Fournier, A., 2010. Fast torsional waves and strong magnetic field within the Earth's core, *Nature,* **465**(7294), 74–77.

Gillet, N., Jault, D., Finlay, C.C. & Olsen, N., 2013. Stochastic modeling of the Earth's magnetic field: inversion for covariances over the observatory era, *Geochem. Geophys. Geosyst.,* **14**(4), 766–786.

Gillet, N., Jault, D. & Finlay, C.C., 2015. Planetary gyre, time-dependent eddies, torsional waves, and equatorial jets at the Earth's core surface, *J. geophys. Res.,* **120**(6), 3991–4013.

Hide, R., Boggs, D.H. & Dickey, J.O., 2000. Angular momentum fluctuations within the Earth's liquid core and torsional oscillations of the core–mantle system, *Geophys. J. Int.,* **143**(3), 777–786.

Jackson, A., Bloxham, J. & Gubbins, D., 1993. Time-dependent flow at the core surface and conservation of angular momentum in the coupled core-mantle system, in *Dynamics of Earth's Deep Interior and Earth Rotation,* pp. 97–107, eds Le Mouël, J.-L., Smylie, D.E. & Herring, T., American Geophysical Union.

Jackson, A., Jonkers, A.R.T. & Walker, M.R., 2000. Four centuries of geomagnetic secular variation from historical records, *Phil. Trans. R. Soc. Lond., A.: Math. Phys. Eng. Sci.,* **358**(1768), 957–990.

Jault, D. & Finlay, C., 2015. Waves in the core and mechanical core-mantle interactions, in *Treatise on Geophysics,* Vol. 8, pp. 225–245, ed. Schubert, G., Elsevier Science.

Jault, D. & Légaut, G., 2005. Alfvén waves within the Earth's core, in *Fluid Dynamics and Dynamos in Astrophysics and Geophysics,* pp. 277–293, eds Soward, A.M., Jones, C.A., Hugues, D.W. & Weiss, N.O., CRC Press.

Jault, D., Gire, C. & Le Mouel, J.L., 1988. Westward drift, core motions and exchanges of angular momentum between core and mantle, *Nature,* **333**(6171), 353–356.

Lewis, H.R. & Bellan, P.M., 1990. Physical constraints on the coefficients of Fourier expansions in cylindrical coordinates, *J. Math. Phys.,* **31**(11), 2592–2596.

Li, K., Livermore, P.W. & Jackson, A., 2010. An optimal Galerkin scheme to solve the kinematic dynamo eigenvalue problem in a full sphere, *J. Comput. Phys.,* **229**(23), 8666–8683.

Mound, J. & Buffett, B., 2007. Viscosity of the Earth's fluid core and torsional oscillations, *J. geophys. Res.,* **112,** B05402, doi:10.1029/2006JB004426.

Mound, J.E. & Buffett, B.A., 2003. Interannual oscillations in length of day: implications for the structure of the mantle and core, *J. geophys. Res.,* **108,** 2334, doi:10.1029/2002JB002054.

Mound, J.E. & Buffett, B.A., 2005. Mechanisms of core-mantle angular momentum exchange and the observed spectral properties of torsional oscillations, *J. geophys. Res.,* **110,** B08103, doi:10.1029/2004JB003555.

Olver, F.W.J., 2010. *NIST Handbook of Mathematical Functions,* Cambridge Univ. Press.

Roberts, P.H. & Aurnou, J.M., 2012. On the theory of core-mantle coupling, *Geophys. astrophys. Fluid. Dyn.,* **106**(2), 157–230.

Schaeffer, N., Jault, D., Cardin, P. & Drouard, M., 2012. On the reflection of Alfvén waves and its implication for Earth's core modelling, *Geophys. J. Int.,* **191**(2), 508–516.

Taylor, J.B., 1963. The magneto-hydrodynamics of a rotating fluid and the Earth's dynamo problem, *Proc. R. Soc. Lond., A. Math. Phys. Sci.,* **274**(1357), 274–283.

APPENDIX A: CALCULATION OF THE WKBJ APPROXIMATIONS

Here, we report some details concerning the derivation of the results of Section 5. According to Bender & Orszag (1999) the WKBJ approximation is a valid one if, as $\delta \to 0$

$$\delta |S_{i+1}(s)| \ll |S_i(s)| \tag{A1}$$

where $i \geq 0$ identify the different terms in the WKBJ expansion (36). These conditions ensure that (36) is an asymptotic series in δ as $\delta \to 0$ uniformly for all s in the interval. As we decide to truncate the series at some order N, we must also ensure that the first of the terms $i > N$ we are neglecting is not as important as the terms with $i \leq N$. That is:

$$\delta^N |S_{N+1}(s)| \ll 1. \tag{A2}$$

The two conditions (A1) and (A2) require that each term in the WKBJ expansion is more important than the successive terms and that, as we truncate the series, everything that has been ignored is of negligible importance. The coefficients $S_i(s)$ are obtained by inserting (36) in eq. (40) which leads us to

$$\frac{c'}{\delta}\sum_{i\geq 0}\delta^i S_i' + \frac{c}{\delta}\sum_{i\geq 0}\delta^i S_i'' + \frac{c}{\delta^2}\left(\sum_{i\geq 0}\delta^i S_i'\right)^2 = -\omega^2 m \tag{A3}$$

where we defined $c(s) = m(s)V_A^2(s)$ for convenience. We now match the terms of different order in δ. The order zero equation is obtained by considering the lowest degree in δ that appears in (A3):

$$\frac{c}{\delta^2}(S_0')^2 = -\omega^2 m. \tag{A4}$$

By setting the small parameter δ equal to ω^{-1} we obtain

$$S_0(s) = \pm \mathrm{i}\int \frac{ds}{V_A(s)}. \tag{A5}$$

To next order in δ we have an equation for $S_1(s)$:

$$\frac{c'}{\delta}S_0' + \frac{c}{\delta}S_0'' + \frac{c}{\delta^2}2\delta S_0' S_1' = 0 \tag{A6}$$

which can be solved taking into account (A5) to give:

$$S_1(s) = \ln\sqrt{\frac{V_A(s)}{c(s)}} = \ln\sqrt{\frac{1}{m(s)V_A(s)}}. \tag{A7}$$

Finally, the coefficient $S_2(s)$ can be calculated by solving

$$c' S_1' + c S_1'' + 2c S_0' S_2' + c(S_1')^2 = 0. \tag{A8}$$

For the Jacobi field case we obtain:

$$\omega S_0(s) = \pm \mathrm{i}\left(2\frac{\omega}{\pi}\arcsin(s) + \omega\eta\right) \tag{A9}$$

$$S_1(s) = \ln\left(\sqrt{\frac{2}{\pi}}\frac{1}{s^{3/2}H}\right) \tag{A10}$$

$$\frac{1}{\omega}S_2(s) = \frac{\mathrm{i}}{\omega}\left[\frac{1}{16}\left(\frac{3H}{s} + 25\arcsin(s)\right) + \eta_2\right]. \tag{A11}$$

From this it is clear that, provided $\omega \gg 0$ (which is the assumption behind the WKBJ approximation) and for finite and reasonable values of η and η_2 (to put a reasonable bound one could require that $\omega \gg \eta, \eta_2$) the conditions (A1) and (A2) are fulfilled in the bulk of the domain as we truncate the expansion (36) at order $N = 1$. We can therefore insert (A9) and (A10) in (36) to obtain the WKBJ spatial solution to the torsional wave equation in the case of the Jacobi Alfvén velocity field:

$$\begin{aligned}\zeta_{II}(s) &= \sqrt{\frac{2}{\pi}}\frac{1}{s^{3/2}H}\left[A_c\cos\left(2\frac{\omega}{\pi}\arcsin(s) + \omega\eta\right)\right.\\ &\quad \left. + A_s\sin\left(2\frac{\omega}{\pi}\arcsin(s) + \omega\eta\right)\right]\\ &= \sqrt{\frac{2}{\pi}}\frac{1}{s^{3/2}H}\left[A_+ \mathrm{e}^{\mathrm{i}\left(2\frac{\omega}{\pi}\arcsin(s)+\omega\eta\right)} + A_- \mathrm{e}^{-\mathrm{i}\left(2\frac{\omega}{\pi}\arcsin(s)+\omega\eta\right)}\right]\end{aligned} \tag{A12}$$

where we can choose one of the two forms. For the calculation of the normal modes it is more convenient to make use of the real form, while the complex one is more suited when studying travelling wave type of solutions. Again, we expect (A12) to be a valid approximation in the region that we approximately defined as $s_1 < s < s_2$ and, in the high-frequency regime:

$$\begin{aligned} s_1 &\to 0\\ s_2 &\to 1. \end{aligned} \tag{A13}$$